High Strength Conductive Composites with Plasmonic Nanoparticles Aligned on Aramid Nanofibers

*Jing Lyu, Xinzhi Wang, Lehao Liu, Yoonseob Kim, Ekembu K. Tanyi, Hang Chi, Wenchun Feng, Lizhi Xu, Tiehu Li, Mikhail A. Noginov, Ctirad Uher, Mark D. Hammig, and Nicholas A. Kotov**

Rapidly evolving fields of biomedical, energy, and (opto)electronic devices bring forward the need for deformable conductors with constantly rising benchmarks for mechanical properties and electronic conductivity. The search for conductors with improved strength and strain have inspired the multiple studies of nanocomposites and amorphous metals. However, finding conductors that defy the boundaries of classical materials and exhibit simultaneously high strength, toughness, and fast charge transport while enabling their scalable production, remains a difficult materials engineering challenge. Here, composites made from aramid nanofibers (ANFs) and gold nanoparticles (Au NPs) that offer a new toolset for engineering high strength flexible conductors are described. ANFs are derived from Kevlar macrofibers and retain their strong mechanical properties and temperature resilience. Au NPs are infiltrated into a porous, free-standing aramid matrix, becoming aligned on ANFs, which reduces the charge percolation threshold and facilitates charge transport. Further thermal annealing at 300 °C results in the Au-ANF composites with an electrical conductivity of 1.25×10^4 S cm^{-1} combined with a tensile strength of 96 MPa, a Young's modulus of 5.29 GPa, and a toughness of 1.3 MJ m^{-3}. These parameters exceed those of most of the composite materials, and are comparable to those of amorphous metals but have no volume limitations. The plasmonic optical frequencies characteristic for constituent NPs are present in the composites with ANFs enabling plasmon-based optoelectronic applications.

1. Introduction

Emerging energy,[1–5] transportation,[6,7] military,[7,8] biomedical,[9] electronic,[5,10–12] and other technologies[13,14] create constantly increasing demand for materials with high mechanical strain/stress, electrical conductivity, thermal stability, toxicology, novel optical,[15] and other properties.[6,16,17] In the last decade these needs inspired extensive research on amorphous metals–unique conductors prepared by rapid vitrification of molten alloys of Au, Pd, or Pt.[18–21] Such alloys represent a special class of materials that combine high mechanical and electrical properties (**Table 1**).[22–24] The absence of crystallites, grain boundaries, and dislocations in the amorphous structure results in high strength, elastic strain limit, corrosion resistance, and in some cases, substantial ductility.[18,25–28] Although these materials can be used in nanoscale molding[18] and some other applications that do not require large volumes, they are difficult to utilize due to rapid recrystallization

J. Lyu, X. Wang, L. Liu, Y. Kim, Dr. W. Feng, Dr. L. Xu, Prof. N. A. Kotov
Department of Chemical Engineering
University of Michigan
Ann Arbor, MI 48109, USA
E-mail: kotov@umich.edu

J. Lyu, X. Wang, L. Liu, Y. Kim, Dr. W. Feng, Dr. L. Xu, Prof. N. A. Kotov
Biointerfaces Institute
University of Michigan
Ann Arbor, MI 48109, USA

J. Lyu, L. Liu, Prof. T. Li
School of Materials Science and Engineering
Northwestern Polytechnical University
Xi'an 710072, P. R. China

X. Wang
School of Energy Science and Engineering
Harbin Institute of Technology
Harbin 150001, P. R. China

DOI: 10.1002/adfm.201603230

E. K. Tanyi, Prof. M. A. Noginov
Center for Materials Research
Norfolk State University
Norfolk, VA 23504, USA

Dr. H. Chi, Prof. C. Uher
Department of Physics
University of Michigan
Ann Arbor, MI 48109, USA

M. D. Hammig
Department of Nuclear Engineering and Radiological Sciences
University of Michigan
Ann Arbor, MI 48109, USA

Prof. N. A. Kotov
Department of Materials Science and Engineering
University of Michigan
Ann Arbor, MI 48109, USA

Prof. N. A. Kotov
Department of Biomedical Engineering
University of Michigan
Ann Arbor, MI 48109, USA

Prof. N. A. Kotov
Michigan Center for Integrative Research in Critical Care
2800 Plymouth Road, Ann Arbor, MI 48109, USA

Table 1. Electrical conductivity and mechanical properties of typical amorphous metallic alloys.

Alloy	Electrical conductivity [S cm^{-1}]	Stress [GPa]	Strain [%]	Young's modulus [GPa]	Reference
$Pd_{40}Cu_{30}Ni_{10}P_{20}$	1.85×10^4	1.72	1.87	92	[26,27]
$Au_{55}Cu_{25}Si_{20}$	–	1.0	1.43	69.8	[31]
$Au_{49.5}Ag_{5.5}Pd_{2.3}Cu_{26.9}Si_{16.3}$	–	1.2	1.61	74.4	[31]
$Zr_{41.2}Ti_{13.8}Cu_{12.5}Ni_{10}Be_{22.5}$	2.28×10^4	1.86	1.96	95	[23,32]
$Pd_{81}Cu_5Si_{14}$	1.56×10^4	1.2	2.00	60.1	[33]

processes transforming metallic glasses into 'normal' (meso)-crystalline metals. The strength of amorphous metals decreases rapidly at moderately elevated temperatures that also cause phase transitions. The physical dimensions of conducting elements from amorphous metals are limited to small flakes or disk-shaped foils[29] and their temperature sensitivity creates problems with processing, particularly for complex shapes.[30–33]

Hybrid organic–inorganic nanocomposites represent another more common avenue to address the challenge of high strength conductors. High mechanical properties and fast charge transport is common for many nanoscale conductors. Although the transfer of these properties from nanoscale to macroscale has fundamental threshholds,[34,35] promising nanocomposite conductors have been made in the form of nanocomposite films, free-standing sheets, and fabrics.[36,37] They show promise as wearable electronic devices,[38–40] biosensors,[40–42] high performance batteries,[4,43–47] and neural implants.[39,48–50] While these composites are mostly based on carbon nanostructures, a lot of them were made from metal nanoparticles (NPs).[51–55] However, the metal NP content in these composites is usually low[56] except several cases of hybrid materials specifically designed for high volume fraction of inorganic components.[57,58] Nanocomposites from metal nanostructures are attractive materials for materials design of high strength conductors due to additional plasmonic optical effects and self-assembly phenomena[59] that are useful in optoelectronics. Vacuum-assisted filtration (VAF) and layer-by-layer (LBL) assembly[60] lead to composites with high loading of Au NPs that helps realizing high electrical conductivity attributed to self-organization processes taking place with NPs imbedded in the flexible polymer matrix.[61] Kirigami patterning offers new tools to resolve the materials property conflict between high strain and high conductivity.[62]

In this study, we are seeking new approaches to produce materials with high strength and high conductivity taking advantage of both nanoscale materials that became available only recently and NP self-organization. Here we describe the possibility to prepare a free standing flexible composite material with these parameters made from prototypical metal NPs and aramid nanofibers (ANFs).[63] The latter represent a versatile new building block among nanomaterials[64–67] and were chosen because ANFs inherits from the parent Kevlar nanofibers high chemical/thermal stability and exceptional mechanical performance (stiffness: 109 GPa and strength: 3.6 GPa), high nanoscale porosity of ANF matrixes,[14,68] and the abundance of surface amide groups on ANFs enables further functionalization of the nanofibers and incorporation of other components onto and between aramid chains.[8] Also importantly production of ANFs is easy to scale.

Au-ANF films made by spin-coating were infiltrated with Au NPs by VAF. Although this method does not provide as high degree of structural engineering control of nanocomposites as one can obtain in LBL,[69,70] it is simpler than previously reported fabrication techniques for NP composites.[71] Compared with other high strength high conductance materials, for instance, amorphous metals, this synthetic method does not have severe temperature or volume restrictions. The open porous[72] structure of ANF films reminiscent of cellular forms of graphene[73–76] allows high loading of Au NPs to form an interconnected 3D conductive network that increases their conductivity. The nanoscale fibers present a convenient template onto which NPs can effectively self-assemble[14,77] to produce particle chains that facilitate charge transport. The Au-ANF film demonstrates electric conduction of 1.25×10^4 S cm^{-1}, tensile strength of 96 MPa, Young's modulus of 5.29 GPa, and toughness of 1.3 MJ m^{-3}, properties that are comparable or surpass those of most nanocomposites and many amorphous metals. Besides deformable conductors, plasmonic properties of constituent NPs enable extended optoelectronic properties. In a perspective of fundamental materials science, the nanoscale porosity and fibrous morphology of the ANF matrix opens the door for mesoscale architectonics.[78]

2. Results and Discussion

2.1. Preparation of Au-ANF Composites

An ANF dispersion was prepared according to the previously reported method.[63] It started from the viscous dark red dispersion obtained by adding bulk Kevlar threads into dimethyl sulfoxide (DMSO) in the presence of potassium hydroxide (KOH) (Supporting Information, Figure S1). Weakening of hydrogen bonds combined with strengthening of electrostatic repulsion between the polymer chains, the bulk aramid macroscale fibers can be chemically transformed into nanofibers. Importantly, the hydrophobic attraction and π–π stacking in the polymer backbone limited the extent of this destruction down to the level of individual polymer chains.[63] The diameter of the resulting nanofibers is determined by the equilibrium of total energy of repulsive and attractive forces which makes them similar to supraparticles.[79–81] Transmission electron microscope (TEM) images showed that the average diameter of ANFs after dissolution was about 20 nm and their lengths were in the range of several micrometers (Supporting Information, Figure S1a).

Spin coating was employed for the preparation of the ANF films; this method is particularly convenient for viscous

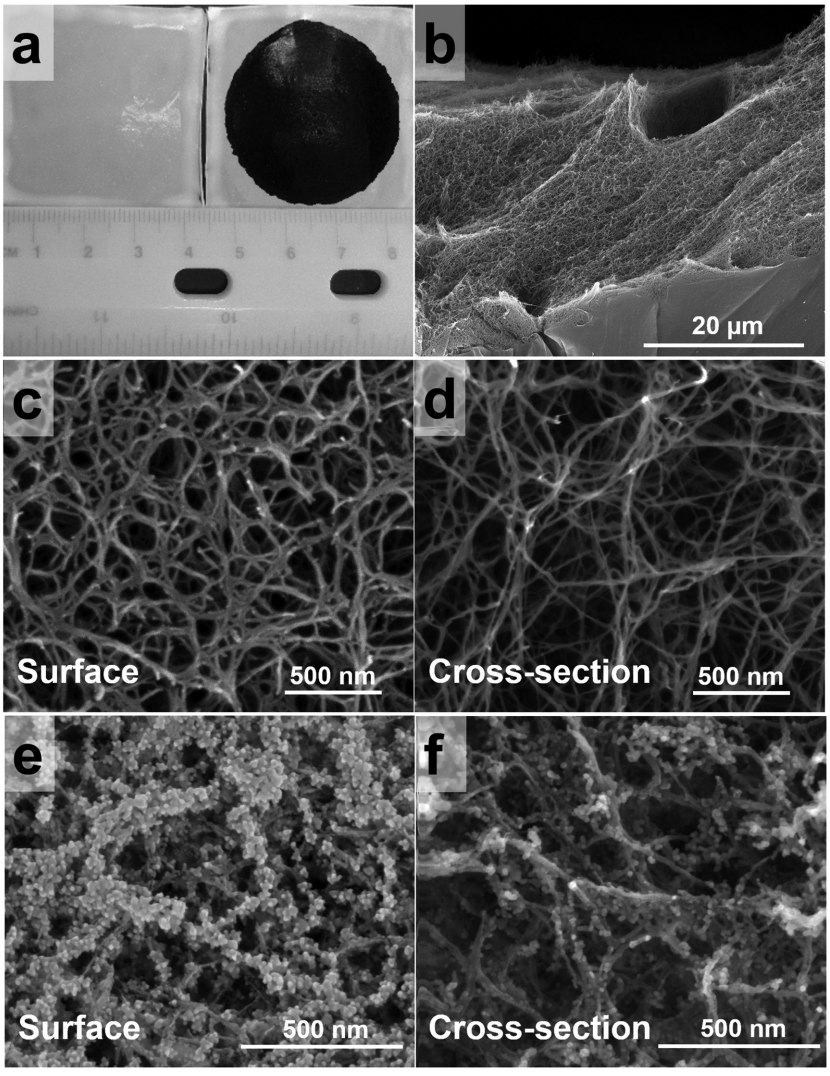

Figure 1. a) Photograph of ANF film and Au-ANF film made using supercritical CO_2 dying. b) Off-angle cross-section SEM image of ANF film. c,d) SEM images of ANF film. e,f) SEM images of Au-ANF film.

dispersions. It makes the film preparation very versatile in controlling the thicknesses of the coatings via tuning the rotation speed and time. The ANF hydrogel films are formed by immersing the films on the glass substrates into deionized water (DI water) to remove the DMSO and protonate ANFs. Fortuitously, the hydrogel spontaneously separated from the substrate during this process. In order to preserve the nanoscale morphology of ANF hydrogels during drying, supercritical CO_2 drying was applied. This is required as the sponge-like structure of the ANF hydrogel can collapse during an ordinary drying process due to the surface tension in the liquid body that pulls against any solid structure with which the liquid might be in contact. The semitransparent, flexible, and porous ANF films formed after supercritical drying are shown in **Figure 1**a (left). Scanning electron microscopy (SEM) images of the microscale morphology of ANF films are shown in Figure 1b–d. A side view cross-sectional image (Figure 1b) shows the sponge-like structure of porous ANF films confirming the open pore structure of the ANF films (Figure 1c,d).

To investigate the thermal stability of ANFs, thermogravimetric analysis (TGA) of Kevlar threads and ANF films were performed at a heating rate of 10 °C min^{-1} under nitrogen atmosphere (Supporting Information, Figure S1b). The TGA curves indicate that the ANF films showed extraordinary thermal stability, similar to the bulk Kevlar threads. This is exciting because thermal stability is necessary to address the bottleneck preventing widespread application of flexible conductors composed of polymer substrates.

Au NPs were synthesized by a citrate-stabilized method because the citrate coating was expected to present a minimal barrier for charge transfer between Au NPs. In addition, the citrate-stabilized Au NPs, about 13 nm in diameter, are well dispersed in aqueous solution, as reported by our group previously (Supporting Information, Figure S2a,b).[61]

At the onset of the study, we incorporated plasmonic Au NPs into ANF films by adsorbing them from a concentrated Au NPs dispersion. Au NPs diffused into the porous films spontaneously and resulted in a measurable volume uptake after a week. From SEM images we could see that Au NPs decorated the surface of ANFs uniformly (Supporting Information, Figure S3). However, this diffusion reached saturation at low volume uptake, which did not enable the films to acquire the desired conductivity. An alternative method, vacuum filtration, was employed to incorporate Au NPs into the ANF films. During this process, ANF films served as the filter membranes into which Au NPs were trapped (Supporting Information, Figure S4a).

Au-ANF films reveal an unambiguous metallic appearance (Figure 1a, right). In order to demonstrate that Au NPs had been trapped within the ANF films, they were subjected to SEM and X-ray diffraction (XRD) analysis. The Au NPs adsorbed along the ANFs throughout the ANF matrix, and an interconnected Au NPs network structure formed (Figure 1e,f). This interconnected network may establish electrical conduction pathways throughout the whole composite if the Au NP volume fraction is sufficiently high throughout the bulk. The XRD patterns of the ANF films and Au-ANF films are shown in Figure S5a of the Supporting Information. The diffraction peaks at 38.1°, 44.2°, 64.5°, and 77.7° were attributed to (111), (200), (220), and (311) planes of a face-centered-cubic (fcc) Au (JCPDS 04–0784).[82] As expected, the XRD peaks indicated that the Au NPs kept the original crystalline domains after being incorporated into the films.

The pore sizes of ANF films are about 200–600 nm, much larger than the diameters of the Au NPs. Initially, all the Au NPs were trapped in the films and then gradually a few Au

NPs passed through the films during vacuum filtration. The adsorption mechanism for citrate covered Au NPs on the ANFs could be explained by hydrogen bonding. The ANF backbones have multitudinous amide groups, each containing a hydrogen atom acting as a hydrogen bound acceptor, while the Au NPs stabilized by citrate are capped by carboxylic acid groups. Upon contact, hydrogen bonding occurs, which binds the Au NPs very tightly to the ANFs (Supporting Information, Figure S4b). FT-IR spectroscopy was carried out to verify this interaction between ANFs and Au NPs. The infrared absorption peaks characteristic of ANFs were observed at 3326 cm^{-1} (N—H stretching vibrations), 1650 cm^{-1} (C=O stretching vibrations), 1545 cm^{-1} (N—H deformation), and 1516 cm^{-1} (C=C stretching vibrations).[63] After incorporation of Au NPs, a broad peak around 3300 cm^{-1} (O—H stretching vibrations) was observed, indicative of the formation of hydrogen bonds (N—H···O). In addition, the IR band of C=O bonds shifts to lower frequency (1640 cm^{-1}) because of the hydrogen bonds formed by C=O groups with N—H groups (Supporting Information, Figure S5b).[83]

2.2. Spectroscopic Studies

The reflectance and absorbance spectra of ANF films and Au-ANF films with different Au concentrations (15.7, 3.4, and 1.0 vol%) were measured. The characteristic onset of bulk Au reflectance (Supporting Information, Figure S6a) was observed in all three Au-ANF films—more pronounced at high concentration of Au NPs, and still seen in samples with low Au concentration (Supporting Information, Figure S7). At high Au concentration, the film's transmission was nearly equal to zero, as expected of thick bulk metallic films. At the same time, the absorbance band characteristic of plasmon resonance in individual Au NPs (Supporting Information, Figure S6b) was observed at lower Au concentrations (**Figure 2**a). None of the signature metallic responses depicted in Au-ANF films was shared by the pure ANF films (Figure 2b). (Sharp edge of absorbance at ≈0.42 μm is related to the onset of the strong absorption band at ≤0.4 μm).

The fact that in the Au-ANF films with low concentrations of Au NPs (Figure 2a and Supporting Information, Figure S7b), the reflectance spectra were characteristic of bulk gold and the absorbance spectra were characteristic of individual Au NPs with typical plasmon band at ≈545 nm was surprising. However, it can be understood taking into account that (1) The reflectance measurements probe the sample's surface, which has a higher concentration of Au NPs, while the transmittance measurements probe the volume, where the concentration of Au NPs is lower; and (2) transmitted and reflected photons experience different numbers of scattering events. Therefore, the transmittance and reflectance measurements probe the same ANF films in different ways, which may explain the seemingly paradoxical coexistence of metallic bulk and plasmonic NP properties.

2.3. Electrical Properties of Au-ANF Films

The pure ANF films are insulators but the introduction of Au NPs relsults in highly conductive hybrid Au-ANF composite films. This transition from insulator to conductor is attributed to the formation of conductive pathways within the composite. Similarly to the previous studies of composite materials with some degree of axial organization of NPs into bands and chains, the present samples show much improved electrical transport[14,51,55,61,84,85] as well as interesting optical properties originating from plasmonic effects.[52,53,86,87]

To further demonstrate the electrical properties of these Au-ANF films, we measured the electrical conductivity as a function of Au volume fraction from 13.9 to 34.7 vol%. The volume fraction of Au NPs can be simply controlled by adjusting the volume of the Au NP solution during the vacuum filtration procedure (Supporting Information, Figure S8a). The electrical conductivity increases with Au NPs loading into the ANF matrices (**Figure 3**a). At an Au content of 13.9 and 14.7 vol%, the composite films did not show any pronounced electrical conductivity. With an increased Au content to 15.7 and 19.6 vol%, a sharp rise in the conductivity was observed. At 15.7 vol%, and 19.6 vol%, the conductivities were 9.64×10^{-4} and 25.36 S cm^{-1}, respectively. Further increased Au loading to 24.8 and 28.9 vol% led to raised conductivities to 114.33 and 204.31 S cm^{-1}, respectively. At an Au concentration of 34.7 vol%, the conductivity reached a value of 1.03×10^3 S cm^{-1}. This trend in the electrical conductivity with respect to Au NPs loading can be explained using percolation theory, which describes the transition from a state of spatially restricted connections of conductive elements to a state of infinite network connections. When the conductive filler volume fraction is low, the average distance between metal particles is so large that conduction was restricted. But when the conductive filler reached a critical concentration, a physical path was formed, through which the current could flow by percolating the entire system. In the vicinity of the transition, the electrical conductivity of the composite increases by orders of magnitude which is expressed via a power-law relationship used in classical percolation theory

$$\sigma = \sigma_0 \left(V_f - V_0\right)^t \quad (1)$$

where σ_0 is the conductivity of the filler, V_0 is the critical concentration or percolation threshold, V_f is the volume fraction of the filler, and t is the critical exponent.[88]

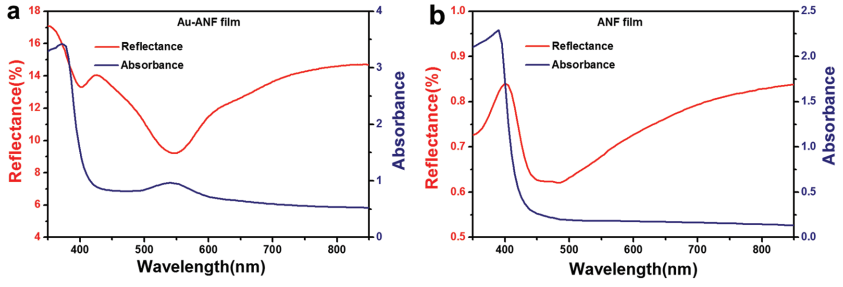

Figure 2. Reflectance and absorbance spectra of a) ANF film and b) Au-ANF film with 1.0 vol% Au NPs.

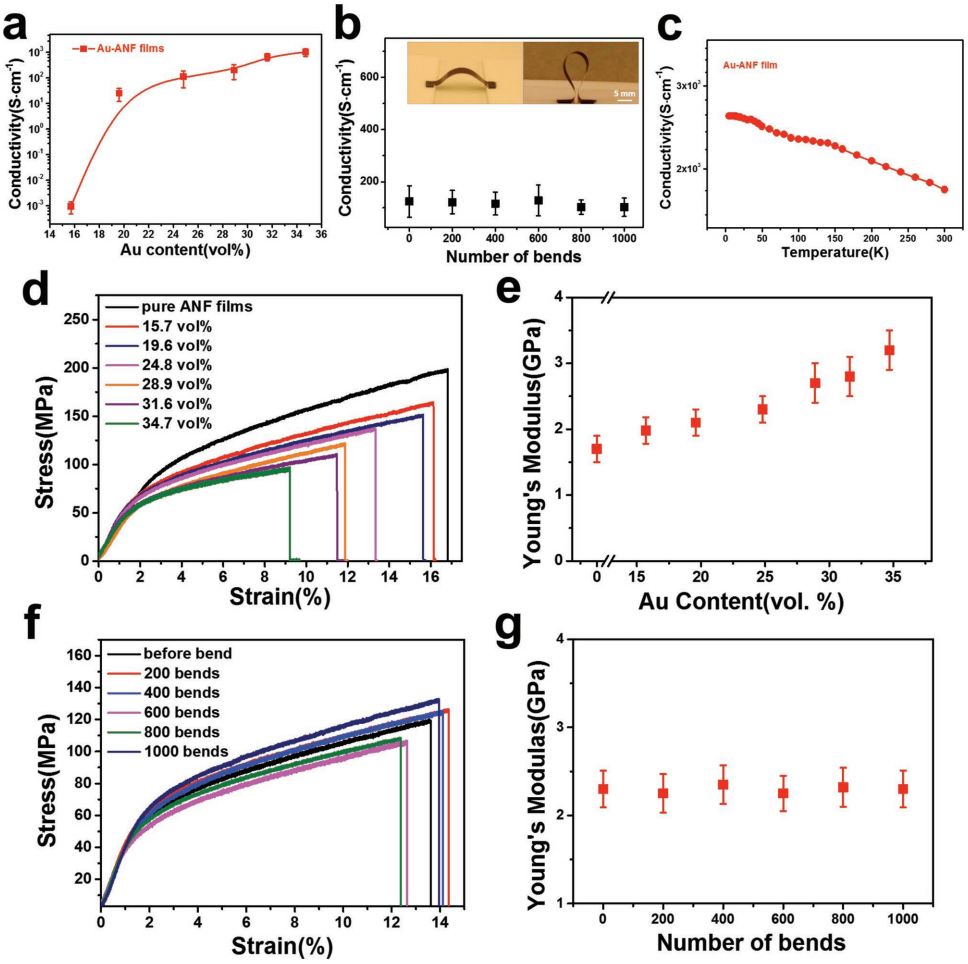

Figure 3. a) The conductivity of Au-ANF films as a function of Au NPs volumetric fraction. b) The conductivity versus number of bends for Au-ANF film with 24.8 vol% Au fraction. c) Temperature dependence of conductivity for Au-ANF films. d,e) The tensile stress and Young's modulus of Au-ANF films with different Au NP volumetric fractions. f,g) The tensile stress and Young's modulus of Au-ANF film (24.8 vol% Au) as a function of number of bends.

Importantly, the experimentally determined value for the percolation threshold of the Au NP-ANF system is 15.7 vol% (Figure 3a), which can be compared to 18.3% for a randomly packed network of spheres.[89] The reduction of the percolation threshold can be attributed to the alignment of NPs on the constituent nanofibers.

The investigation of the mechanisms of conduction in Au-ANF films is both academically and practically significant. The conductivity linearly declines with increasing temperature from 5 to 300 K indicating metallic conduction behavior. Figure 3c shows the temperature dependence of the conductivity for supercritical dried Au-ANF films. Fitting the temperature dependence of conductivity with variable-range hopping and tunneling conduction mechanism equations revealed that the electron transfer mechanism was not dominated in this manner (Supporting Information, Figure S9).

2.4. Mechanical Properties of Au-ANF Films

The mechanical properties of Au-ANF films are critical for the design of devices. We found that the Au-NPs composites combine high electrical conductivity and high strength. However, the tensile strength gradually decreases with the increase in the Au NPs volumetric fraction (Figure 3d). The maximum tensile strength decreased from 196 MPa (pure ANF films) to 96 MPa (34.7 vol% Au NPs). However, the Young's modulus increased from 1.7 to 3.2 GPa with an increase Au NPs concentration (Figure 3e). The optimization between the electrical conductivity and tensile properties of the nanocomposite can be realized by properly controlling the Au NPs volumetric fraction.

The maximum tensile strength of Au-ANF composite films depends on the weakest fracture path throughout the films. Au NPs are likely to affect the tensile strength via two opposing mechanisms. One is a weakening effect due to the NP-induced stress concentration, and the second is a reinforcing effect since they may serve as barriers to crack growth. In this case, the weakening effect is predominant, thus the Au-ANF films strength is lower than that of the pure ANF films.[90] The strain at break decreased with the increase in Au NP volumetric fraction as well. This is due to the interactions between Au NPs and the ANF matrix, which restricts the movement of polymer chains. This behavior is typical of polymer composites reinforced with fillers of nanoscale dimension.[91] Generally, the

addition of higher amounts of filler content to polymers leads to poor processability and inferior mechanical performance.[92]

Flexibility is significant for high-strength conductor to be employed in wearable electronics[93] and other applications. A film with Au content of 24.8 vol% was subjected to tension bending (Figure 3b inset). The Au-ANF film exhibited excellent mechanical flexibility; there was no significant change in electrical conductivity even after 1000 bending cycles, and the tensile stress and Young's modulus remained unchanged within experimental error (Figure 3f,g).

2.5. Thermal Annealing

Exploiting the high temperature stability of ANFs, the conductivity of Au-ANF films can be improved by thermal annealing. This enhances the crystallinity of, and connectivity between, metal NPs[94] at temperatures unsuitable for other polymers. Based on TGA results of ANF films and Au-ANF films (Supporting Information, Figures S1b and S8), we believe that ANFs will remain stable at temperatures as high as 400 °C. The coalescence of Au NPs can be achieved at temperatures of ≈10% of the melting points of their bulk counterparts (1336 K), due to their high surface area to volume ratio and surface atom instability.[95] In addition, at above 175 °C, the citrate stabilizer decomposed into H_2O and CO_2, which migrated away from the inter-particle regions and improved contact between the Au NPs.[96] Considering these observations, thermal annealing temperatures between 200 and 400 °C were employed.

The conductivity of Au-ANF films with 34.7 vol% Au content improved with increasing annealing temperature, rising from 1.03×10^3 to 1.25×10^4 S cm^{-1} after annealing for 20 min at 300 °C. Increasing the annealing temperature to 400 °C, the conductivity reached 6.3×10^4 S cm^{-1} (**Figure 4**a).

The increased intensities of the XRD peaks provided evidence that thermal annealing improved the Au NPs crystallinity. Figure 4b shows the XRD patterns of the as-prepared Au-ANF film with 34.7 vol% Au content and the films obtained by annealing under temperatures ranging from 200 to 400 °C. All of the films exhibited the indexed diffraction peak consistent with the standard values of a face-centered-cubic (fcc) Au structure (JCPDS 04–0784). As annealing temperatures increased from 200 to 400 °C, the Au(111), Au(200), Au(220), and Au(311) peaks increased their amplitude and decreased their full width at half maximum (FWHM) as a result of a gradual improvement in crystallinity and reduced crystal defects.[94] The average crystallite size of Au NPs calculated from the Scherrer equation increased from 14.8 nm to 20.5 nm after annealing (Supporting Information, Table S1), which was in agreement with the SEM images (Figure 4e–j).

While thermal annealing increases conductivity, that improvement came at the expense of a decrease in ultimate strain,[95] which dropped from 9.2% to 1.0%. The tensile strength of the Au-ANF films was maintained at about 95 MPs at temperatures under 300 °C (Figure 4c), while the Young's modulus increased from 3.07 to 5.29 GPa (Figure 4d). When the annealing temperature exceeded 300 °C, the tensile strength and Young's modulus tended to decrease. Figure 4e–j shows SEM images of the Au-ANF films at different annealing temperatures. The microscopy images of the films indicated stronger interparticle coalescence with increased annealing temperatures. When annealed at 200 °C, some of the Au NPs fused into larger NPs (Figure 4f). As the temperature increased to 300 °C, most of the Au NPs coalesced and formed irregularly shaped particles (Figure 4h). Increasing the annealing temperature to 400 °C, the irregularly shaped particles fused together to form a network throughout the entire Au-ANF films (Figure 4j).[70]

The electrical conductivity and ultimate tensile strength of Au-ANF films are compared with those for nanocomposites (graphene based, CNT based, etc.) and amorphous metals (Ce-based, Pd-based, etc.) in **Figure 5**. The comparison shows that some graphene based nanocomposites, such as graphene/ANF and graphene/cellulose (data points 5 and 6) display electrical conductivity and ultimate strength higher than these of nanocomposites. Electrical conductivity for composites is still 3–4 orders lower than that of Au-ANF films except the LBL-assembled Au NPs/PU composite that exhibits high electrical conductivity, but lower ultimate strength to Au-ANF films. The amorphous metals display higher ultimate strength with comparable electrical conductivity, however, the limited process-zone size restricts the structural use of amorphous metals to small components.

The observed conductivity of Au NP-ANF composites is most likely lower than the maximum performance possible. Conductivity can be improved by maximizing the uniformity of the conductance throughout the film depth. Although Au NPs are incorporated throughout the cross-section of the Au-ANF films (Supporting Information, Figure S10), the electrical characterization of the films indicated that the volume fraction of Au NPs in the bulk is below the critical volume fraction necessary to percolate metallic-conduction through the entire film thickness. The alignment of NPs along ANF fibers makes charge transport possible, but can still be optimized further. **Figure 6**a,b shows the current–voltage (*IV*) characteristics for the 24.8 vol% annealed film when probed either along the top surface (Figure 6a) or across the bulk (Figure 6b). Probing the top surface exhibits metallic conduction with lower resistivity as the annealing temperature was increased, while the bulk resistivity remained high regardless of the temperature conditioning, indicating that the bulk current leakage is roughly 10 orders of magnitude smaller than the surface current.

The formation of a conducting composite upon the insulating ANF network is also demonstrated in the capacitance–voltage (CV) curves of Figure 6c. The measured capacitances, in the range of 4 pF, from the ≈2×2 mm^2 areal contact were consistent with that expected from a parallel plate capacitor bounding a mixed air ($C_{\text{pure air}}$ = 4.7 pF) and Kevlar ($C_{\text{bulk Kevlar}}$ = 18.8 pF) dielectric. Possessing a means of control over the penetration depth of the conductive layer opens up the possibility of using the Au-ANF structure in a metal–insulator configuration, for use in high voltage capacitors or metal–insulator–metal sensors, as we could apply over 800 V to the film without breakdown-induced damage.

3. Conclusions

Au NPs were incorporated into a porous ANF matrix to realize materials with high strength and high electrical conductivity;

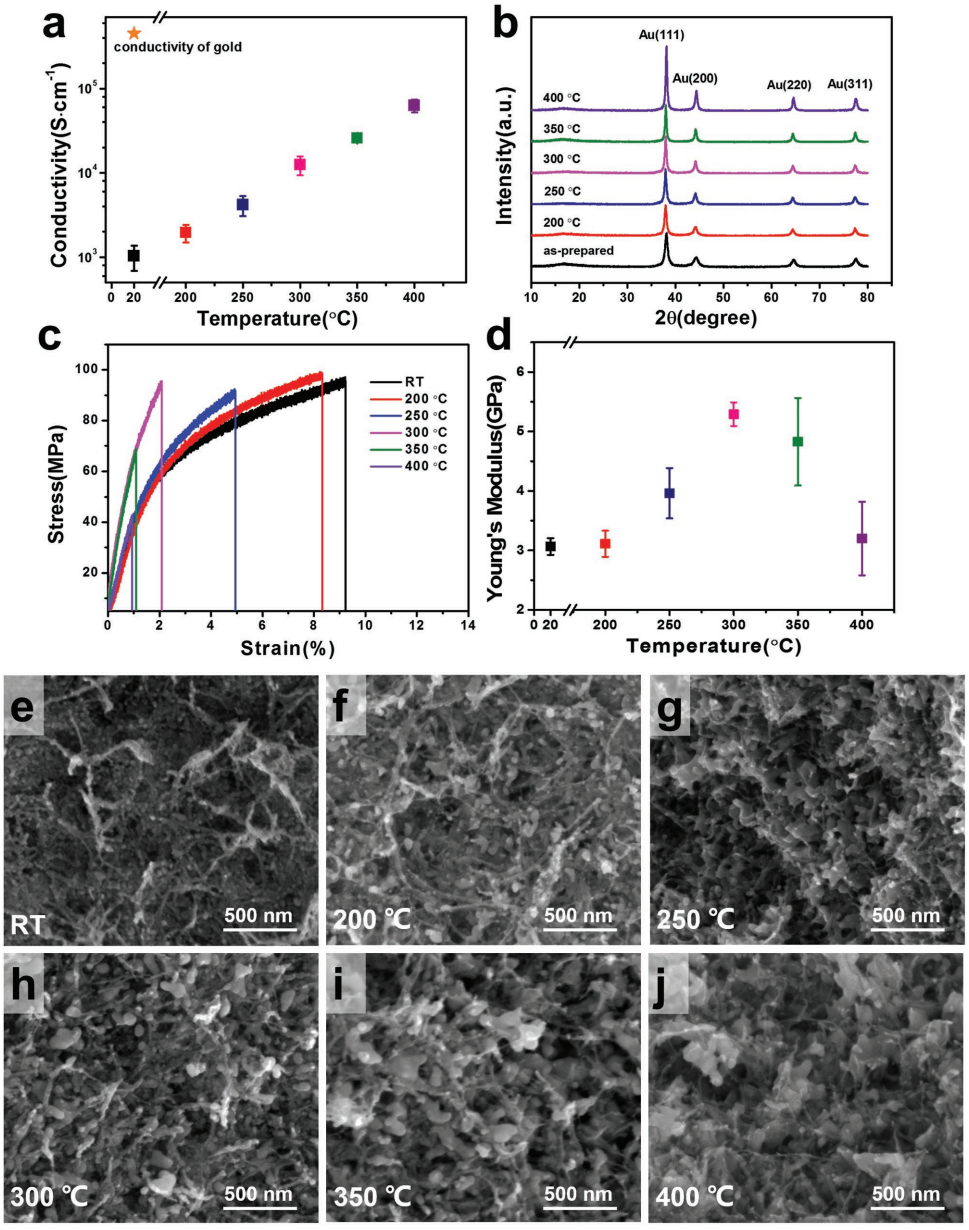

Figure 4. a) Electrical conductivity of supercritical dried Au-ANF films as a function of annealing temperatures (black – 20 °C, red – 200 °C, blue – 250 °C, pink – 300 °C, green – 350 °C, purple – 400 °C). b) XRD patterns of the as-prepared Au-ANF films and the annealed Au-ANF films at various temperatures. c) The stress–strain curves of supercritical dried Au-ANF films with different annealing temperatures. d) Young's modulus of supercritical dried Au-ANF films with different annealing temperatures. e–j) SEM images of supercritical dried Au-ANF films at different annealing temperatures.

higher and higher values for both are needed among other applications for flexible electronics, energy storage devices, and biological implants. The unusually high combination of these properties with is difficult to attain and in ANF-NP composites it was enabled by the high-strength ANF network serving as a backbone for assembly and the alignment of Au NPs. The mechanical and electrical properties of ANF-NP composites are comparable to amorphous metals while avoiding difficulties with processing, scalability, and brittleness. The Au-ANF composite films also demonstrate flexibility, creating a viable alternative to other flexible conductors based on nanoscale carbons (CNTs and graphene) or metallic nanowires. Future studies involving the design and engineering of high-performance polymeric composites may include the use of other plasmonics and metals in nanoscale form such as copper and silver NPs.

4. Experimental Section

Chemicals: Tetrachloroaurate (III) trihydrate ($HAuCl_4 \cdot 3H_2O$), sodium citrate tribasic dihydrate ($Na_3C_6H_5O_7 \cdot 2H_2O$), dimethyl sulfoxide (DMSO), and potassium hydroxide (KOH) were all purchased from Sigma-Aldrich and used as received. Bulk Kevlar 69 was purchased from Thread Exchange. E-pure deionized water (18.2 MΩ cm^{-1}) was obtained from a Millipore Milli-Q system. Glass slides (50 mm × 50 mm, Corning) were cleaned with piranha solution (3:1 v/v H_2SO_4/H_2O_2).

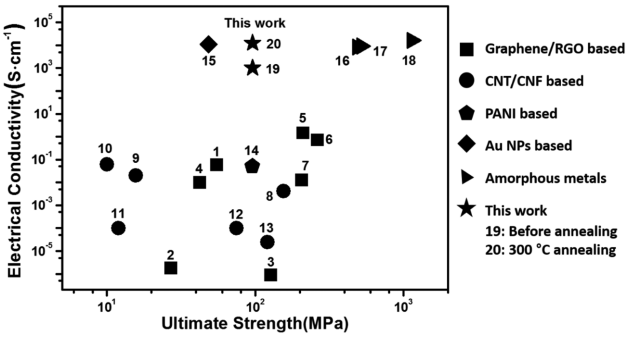

Figure 5. Comparison of electrical conductivity and ultimate strength of Au-ANF composite films with selected conductive nanocomposites (graphene based, carbon nanotube based, etc.) and amorphous metals.[61,66,97–112] 1: graphene/PVC;[97] 2: graphene/polypropylene;[98] 3: graphene/polyimide;[99] 4: RGO/PVDF;[100] 5: graphene/ANF;[66] 6: graphene/cellulose;[101] 7: RGO/chitosan;[102] 8: CNT/PPE;[103] 9: CNT/polyethylene;[104] 10: MWNT/epoxy;[105] 11: MWNT/polyethylene;[106] 12: CNF/epoxy;[107] 13: MWNT/polyimide;[108] 14: PANI/bacterial cellulose;[109] 15: Au NPs/polyurethane;[61] 16: $Ce_{70}Al_{10}Cu_{20}$ or $Ce_{68}Al_{10}Cu_{20}Nb_2$ amorphous alloys;[110] 17: Al–Ln amorphous alloys;[111] 18: $Pd_{76}Cu_7Si_{17}$ thin film metallic glasses;[112] 19: Au-ANF film with 34.7 vol% Au content, 20: Au-ANF film after 300 °C thermal annealing.

Synthesis of Au NPs: Our synthesis route is straightforward. Typically, gold (III) chloride trihydrate (90.0 mg) was introduced into 475 mL ultrapure deionized water in a glass beaker with appropriate volume equipped with a magnetic stirring bar. The solution was heated to boiling under vigorous stirring followed by additional heating for 20 min. Subsequently, 25 mL of 1.0 wt% sodium citrate solution was added to the gold salt solution. The mixture was heated for 20 min to produce a wine red colored, stable solution, which was cooled to room temperature.

Preparation of ANF Films: 10.0 g of bulk Kevlar 69 was dissolved in DMSO with 10.0 g KOH to obtain a 2 wt% ANF solution, which was then magnetically stirred for three weeks at room temperature until a dark red, viscous solution formed.

Spin coating was applied to deposit the ANF films. Glass slides were cleaned with piranha solution, followed by thoroughly rinsing with DI water and compressed air-drying. After setting the glass slide on the disk of the spin coater, 3 mL of ANF solution was dropped and spin-coated at 600 rpm for 30 s. After spin coating, the films were immediately put into DI water to remove the DMSO.

Preparation of Au-ANF Films with Vacuum Filtration (VF): The Au NP solution was forced to penetrate into the ANF films through the vacuum filtration process illustrated in Figure S4a of the Supporting Information. The Au-ANF films with various Au content were prepared under the same conditions and procedures except for the volume of Au NPs solution. Au-ANF films containing 13.9, 14.7, 15.7, 19.6, 24.8, 28.9, 31.6, and 34.7 vol% of Au consumed 180, 190, 200, 250, 350, 450, 550, and 650 mL of Au NP solution, respectively. The obtained films were subsequently dried in a supercritical CO_2 dryer. The films were dehydrated with ethanol followed by soaking in liquid CO_2 to exchange the pore fluid inside the films with liquid CO_2. Subsequently, the liquid CO_2 was heated to reach the critical point, after which the supercritical CO_2 was slowly decompressed to atmospheric pressure.

Annealing of Au-ANF Films: The prepared Au-ANF films were placed in a muffle furnace and annealed at different temperatures (200, 250, 300, 350, and 400 °C) for 20 min.

Characterizations: TEM images were collected by a JEOL 3011 HRTEM. One drop of solution (10 µL) was placed on the surface

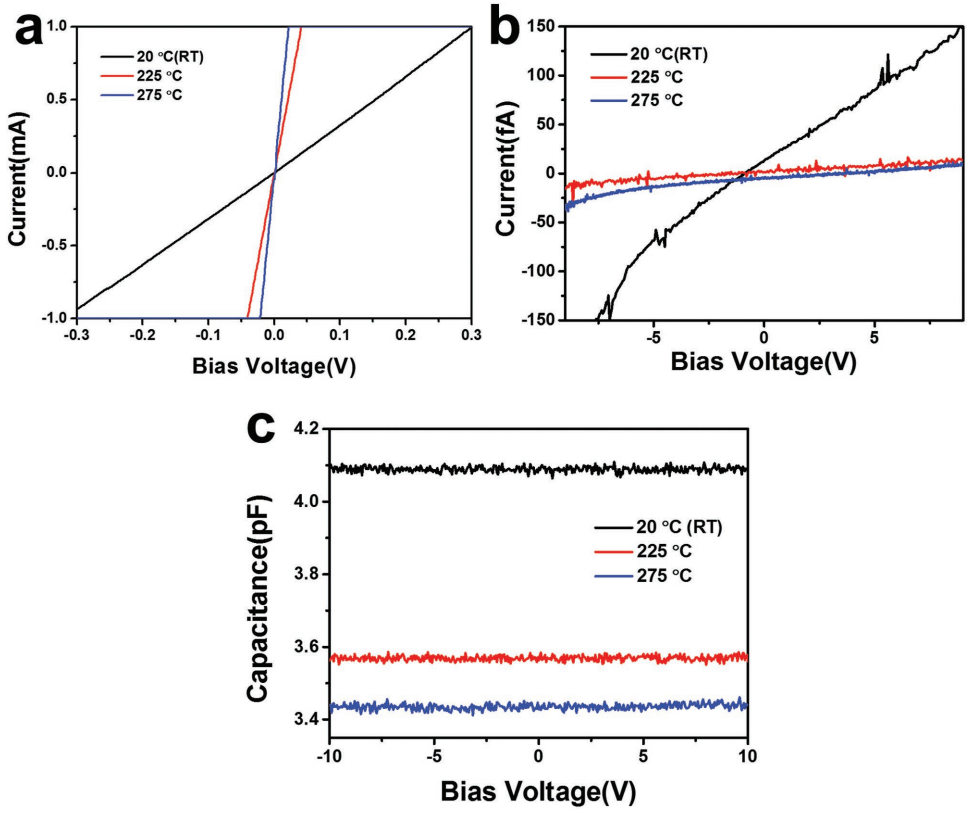

Figure 6. a) Surface *IV* characteristic measured by probing the top-side surface of the film for room temperature and two annealed samples. b) Bulk *IV* characteristic measured by probing from the top of the film to the bottom. c) CV measured across the bulk of the nonannealed and two annealed films.

of a copper grid coated with carbon and dried before testing. The morphologies of ANF films and Au-ANF films were inspected with a FEI Nova Nanolab dual-beam FIB and scanning electron microscope. The distribution of Au NPs in the Au-ANF films were analyzed with an energy-dispersive X-ray spectroscopy (EDS) mapping conducted in the SEM's EDAX mode (Supporting Information, Figure S10). The Au-ANF film's Au fractions were determined by a TA Instruments Discovery Thermogravimetric Analyzer (TGA) with a temperature ramp to 700 at 10 °C min^{-1} in nitrogen at a flow rate of 25 mL min^{-1}. XRD patterns of Au NPs, ANF films, and Au-ANF films were collected at ambient temperature using Rigaku Rotating Anode X-Ray Diffractometer with Cu K_α generated at 40 kV and 100 mA. XRD patterns were processed in MDI Jade 5.0 to calculate peak positions, intensity, and full width at half maximum. Fourier transform infrared spectroscopy (FT-IR) was performed on a Nicolet 6700 spectrometer to investigate the chemical properties of Au-ANF films. The samples for FT-IR tests were prepared by spin-coating 1 wt% ANF solutions to obtain ultrathin films with good transmittance. The tensile property of each film was determined using a TA XT Plus Texture Analyzer (Stable Micro Systems Ltd.). The samples were cut into rectangular strips of ≈20 mm × 2 mm using a razor blade and five strips were measured for each film. Conductivity measurements with two- and four-probe methods were acquired using a Lucas S-302-4 four points probe station with the Agilent 34401A multimeter. The thickness of Au-ANF films was determined by cross-section SEM images to be ≈7.5 µm. A series of five measurements were taken for each film and the data were averaged to give the final reported values. Error bars indicate one standard deviation for the five measurements. The temperature dependence of conductivity measurements was performed from 5 to 300 K in a quantum design magnetic property measurement system (MPMS), equipped with a 5.5 T superconducting magnet, using a Linear Research ac bridge with 16 Hz excitation. The reflectance and transmittance spectra of ANF films and Au-ANF films were measured using the Lambda 900 spectrophotometer equipped with the 150 mm integrating sphere (PerkinElmer). The samples were mounted on the back of the integrating sphere. The angle of incidence light was equal to 8°. The reflected light, which had a large diffuse component, was detected by a photomultiplier tube (PMT) installed in the bottom of the integrating sphere. A standard white diffuse reflector (from Labsphere) was used as a 100% reference. The IV and CV curves were acquired using a Keithley 4200-SCS semiconductor parameter analyzer and were measured from −10 V to +10 V, in steps of 0.05 V at five different sweep frequencies (100 kHz, 1 MHz, 2 MHz, 5 MHz, and 10 MHz) using a 100 mV_{RMS} drive voltage. The capacitance does not vary for probe frequencies below 1 MHz which was the frequency used to plot the data in Figure 5c.

Supporting Information

Supporting Information is available from the Wiley Online Library or from the author.

Acknowledgments

The central part of this work was supported by the NSF project "Energy- and Cost-Efficient Manufacturing Employing Nanoparticles" NSF 1463474. Partial support of this work was also made by the Center for Photonic and Multiscale Nanomaterials (C-PHOM) funded by the National Science Foundation (NSF) Materials Research Science and Engineering Center program DMR1120923 as well as NSF Projects 1403777, 1411014, 1463474, and 1538180. The authors acknowledge the financial assistance by the China Scholarship Council to J.L, X.W., and L.L. The authors thank the University of Michigan's EMAL for its assistance with electron microscopy, and for the NSF grant #DMR-9871177 for funding of the JEOL 2010F analytical electron microscope used in this work. The Norfolk State University portion of this work was supported by the NSF PREM grant DMR-1205457, NSF IGERT grant DGE-0966188, HBCU RISE grant NSF HRD-1345215 and ARO grant W911NF-14-1-0639. Additional support was provided by the Basic Research and Applied Research Programs of the US Department of Defense's Defense Threat Reduction Agency (HDTRA-1-11-1-0050, HDTRA1-12-1-0038, HDTRA1-13-C- 0050), as well as the US Department of Homeland Security, Domestic Nuclear Detection Agency (2015-DN-077-097). This support does not constitute an express or implied endorsement on the part of the government. The M-Cube collaboration funds from Universirt of Michigan are gratefully acknowledged.

Received: June 28, 2016
Revised: August 20, 2016
Published online: October 21, 2016

[1] Y. Li, T. Yu, T. Yang, L. Zheng, K. Liao, *Adv. Mater.* **2012**, *24*, 3426.
[2] Y. Cheng, S. Lu, H. Zhang, C. V. Varanasi, J. Liu, *Nano Lett.* **2012**, *12*, 4206.
[3] X. Xiao, T. Li, P. Yang, Y. Gao, H. Jin, W. Ni, W. Zhan, X. Zhang, Y. Cao, J. Zhong, *ACS Nano* **2012**, *6*, 9200.
[4] R. Mo, S. O. Tung, Z. Lei, G. Zhao, K. Sun, N. A. Kotov, *ACS Nano* **2015**, *9*, 5009.
[5] M. A. Worsley, S. O. Kucheyev, J. D. Kuntz, T. Y. Olson, T. Y.-J. Han, A. V. Hamza, J. H. Satcher, T. F. Baumann, *Chem. Mater.* **2011**, *23*, 3054.
[6] J. N. Coleman, U. Khan, Y. K. Gun'ko, *Adv. Mater.* **2006**, *18*, 689.
[7] R. Baughman, C. Cui, A. Zakhidov, Z. Iqbal, J. Barisci, G. Spinks, G. Wallace, A. Mazzoldi, D. De Rossi, A. Rinzler, O. Jaschinski, S. Roth, M. Kertesz, *Science* **1999**, *284*, 1340.
[8] I. O'Connor, H. Hayden, J. N. Coleman, Y. K. Gun'ko, *Small* **2009**, *5*, 466.
[9] E. Jan, J. L. Hendricks, V. Husaini, S. M. Richardson-Burns, A. Sereno, D. C. Martin, N. A. Kotov, *Nano Lett.* **2009**, *9*, 4012.
[10] Y. Zhou, S.-T. Han, Z.-X. Xu, V. A. L. Roy, *Nanotechnology* **2012**, *23*, 344014.
[11] S. Park, M. Vosguerichian, Z. Bao, *Nanoscale* **2013**, *5*, 1727.
[12] T. Sekitani, U. Zschieschang, H. Klauk, T. Someya, *Nat. Mater.* **2010**, *9*, 1015.
[13] P. Podsiadlo, A. K. Kaushik, E. M. Arruda, A. M. Waas, B. S. Shim, J. Xu, H. Nandivada, B. G. Pumplin, J. Lahann, A. Ramamoorthy, N. A. Kotov, *Science* **2007**, *318*, 80.
[14] H. Qian, A. Bismarck, E. S. Greenhalgh, G. Kalinka, M. S. P. Shaffer, *Chem. Mater.* **2008**, *20*, 1862.
[15] A. V. Kildishev, A. Boltasseva, V. M. Shalaev, *Science* **2013**, *339*, 1232009.
[16] X. Zhang, Q. Li, T. G. Holesinger, P. N. Arendt, J. Huang, P. D. Kirven, T. G. Clapp, R. F. DePaula, X. Liao, Y. Zhao , L. Zheng, D. E. Peterson, Y. Zhu, *Adv. Mater.* **2007**, *19*, 4198.
[17] B. S. Shim, J. Zhu, E. Jan, K. Critchley, N. A. Kotov, *ACS Nano* **2010**, *4*, 3725.
[18] G. Kumar, H. X. Tang, J. Schroers, *Nature* **2009**, *457*, 868.
[19] J. Schroers, B. Lohwongwatana, W. L. Johnson, A. Peker, *Appl. Phys. Lett.* **2005**, *87*, 61912.
[20] B. E. Schuster, Q. Wei, M. H. Ervin, S. O. Hruszkewycz, M. K. Miller, T. C. Hufnagel, K. T. Ramesh, *Scr. Mater.* **2007**, *57*, 517.
[21] A. Inoue, *Acta Mater.* **2000**, *48*, 279.
[22] J. Basu, S. Ranganathan, *Sadhana* **2003**, *28*, 783.
[23] W. L. Johnson, *JOM* **2002**, *54*, 40.
[24] W.-H. Wang, C. Dong, C. H. Shek, *Mater. Sci. Eng., R* **2004**, *44*, 45.
[25] A. Inoue, *Mater. Sci. Eng., A* **2001**, *304*, 1.
[26] H. Guo, P. F. Yan, Y. B. Wang, J. Tan, Z. F. Zhang, M. L. Sui, E. Ma, *Nat. Mater.* **2007**, *6*, 735.
[27] M. F. Ashby, A. L. Greer, *Scr. Mater.* **2006**, *54*, 321.

[28] C. A. Schuh, T. C. Hufnagel, U. Ramamurty, *Acta Mater.* **2007**, *55*, 4067.
[29] R. Hasegawa, *Mater. Sci. Eng., A* **2004**, *375*, 90.
[30] G. Kumar, A. Desai, J. Schroers, *Adv. Mater.* **2011**, *23*, 461.
[31] M. Chen, *Annu. Rev. Mater. Res.* **2008**, *38*, 445.
[32] M. Yamasaki, S. Kagao, Y. Kawamura, K. Yoshimura, *Appl. Phys. Lett.* **2004**, *84*, 4653.
[33] R. Yamauchi, S. Hata, J. Sakurai, A. Shimokohbe, *Jpn. J. Appl. Phys., Part 1* **2006**, *45*, 5911.
[34] C. Sanchez, B. Julian, P. Belleville, M. Popall, *J. Mater. Chem.* **2005**, *15*, 3559.
[35] A. a. Mamedov, N. a. Kotov, M. Prato, D. M. Guldi, J. P. Wicksted, A. Hirsch, *Nat. Mater.* **2002**, *1*, 190.
[36] J. Jancar, J. F. Douglas, F. W. Starr, S. K. Kumar, P. Cassagnau, a. J. Lesser, S. S. Sternstein, M. J. Buehler, *Polymer* **2010**, *51*, 3321.
[37] A. K. Yetisen, H. Qu, A. Manbachi, H. Butt, M. R. Dokmeci, J. P. Hinestroza, M. Skorobogatiy, A. Khademhosseini, S. H. Yun, *ACS Nano* **2016**, *10*, 3042.
[38] M. Kaltenbrunner, T. Sekitani, J. Reeder, T. Yokota, K. Kuribara, T. Tokuhara, M. Drack, R. Schwödiauer, I. Graz, S. Bauer-Gogonea, S. Bauer, T. Someya, *Nature* **2013**, *499*, 458.
[39] D.-H. Kim, N. Lu, R. Ma, Y.-S. Kim, R.-H. Kim, S. Wang, J. Wu, S. M. Won, H. Tao, A. Islam, K. J. Yu, T.-I. Kim, R. Chowdhury, M. Ying, L. Xu, M. Li, H.-J. Chung, H. Keum, M. McCormick, P. Liu, Y.-W. Zhang, F. G. Omenetto, Y. Huang, T. Coleman, J. A. Rogers, *Science* **2011**, *333*, 838.
[40] G. Schwartz, B. C.-K. Tee, J. Mei, A. L. Appleton, D. H. Kim, H. Wang, Z. Bao, *Nat. Commun.* **2013**, *4*, 1859.
[41] B. S. Shim, W. Chen, C. Doty, C. Xu, N. A. Kotov, *Nano Lett.* **2008**, *8*, 4151.
[42] J. Zhang, M. P. Landry, P. W. Barone, J.-H. Kim, S. Lin, Z. W. Ulissi, D. Lin, B. Mu, A. A. Boghossian, A. J. Hilmer, A. Rwei, A. C. Hinckley, S. Kruss, M. A. Shandell, N. Nair, S. Blake, F. Sen, S. Sen, R. G. Croy, D. Li, K. Yum, J. H. Ahn, H. Jin, D. A. Heller, J. M. Essigmann, D. Blankschtein, M. S. Strano, *Nat. Nanotechnol.* **2013**, *8*, 959.
[43] S.-O. Tung, S. Ho, M. Yang, R. Zhang, N. A. Kotov, *Nat. Commun.* **2015**, *6*, 6152.
[44] A. Vu, A. Stein, *Chem. Mater.* **2011**, *23*, 3237.
[45] H. Huang, S.-C. Yin, T. Kerr, N. Taylor, L. F. Nazar, *Adv. Mater.* **2002**, *14*, 1525.
[46] Y. Liu, M. Zhu, D. Chen, *J. Mater. Chem. A* **2015**, *3*, 11857.
[47] K. Chang, W. Chen, *ACS Nano* **2011**, *5*, 4720.
[48] H. Zhang, P. R. Patel, Z. Xie, S. D. Swanson, X. Wang, N. A. Kotov, *ACS Nano* **2013**, *7*, 7619.
[49] H. Zhang, J. Shih, J. Zhu, N. A. Kotov, *Nano Lett.* **2012**, *12*, 3391.
[50] D.-H. Kim, J. Viventi, J. J. Amsden, J. Xiao, L. Vigeland, Y.-S. Kim, J. A. Blanco, B. Panilaitis, E. S. Frechette, D. Contreras, D. L. Kaplan, F. G. Omenetto, Y. Huang, K.-C. Hwang, M. R. Zakin, B. Litt, J. A. Rogers, *Nat. Mater.* **2010**, *9*, 511.
[51] T. Reuter, O. Vidoni, V. Torma, G. Schmid, L. Nan, M. Gleiche, L. Chi, H. Fuchs, *Nano Lett.* **2002**, *2*, 709.
[52] A. Choudhary, G. Singh, A. M. Biradar, *Nanoscale* **2014**, *6*, 7743.
[53] D. Ryu, K. J. Loh, R. Ireland, M. Karimzada, F. Yaghmaie, A. M. Gusman, *Smart Struct. Syst.* **2011**, *8*, 471.
[54] H. Ismaili, D. Geng, A. X. Sun, T. T. Kantzas, M. S. Workentin, *Langmuir* **2011**, *27*, 13261.
[55] B. Kim, W. M. Sigmund, *Langmuir* **2004**, *20*, 8239.
[56] J. Cai, S. Kimura, M. Wada, S. Kuga, *Biomacromolecules* **2009**, *10*, 87.
[57] H. Schlicke, J. H. Schröder, M. Trebbin, A. Petrov, M. Ijeh, H. Weller, T. Vossmeyer, *Nanotechnology* **2011**, *22*, 305303.
[58] C. Jiang, S. Markutsya, Y. Pikus, V. V. Tsukruk, *Nat. Mater.* **2004**, *3*, 721.
[59] T. Yonezawa, H. Matsune, T. Kunitake, *Chem. Mater.* **1999**, *11*, 33.
[60] K. Ariga, Y. Yamauchi, G. Rydzek, Q. Ji, Y. Yonamine, K. C.-W. Wu, J. P. Hill, *Chem. Lett.* **2014**, *43*, 36.
[61] Y. Kim, J. Zhu, B. Yeom, M. Di Prima, X. Su, J.-G. Kim, S. J. Yoo, C. Uher, N. A. Kotov, *Nature* **2013**, *500*, 59.
[62] T. C. Shyu, P. F. Damasceno, P. M. Dodd, A. Lamoureux, L. Xu, M. Shlian, M. Shtein, S. C. Glotzer, N. A. Kotov, *Nat. Mater.* **2015**, *14*, 785.
[63] M. Yang, K. Cao, L. Sui, Y. Qi, J. Zhu, A. Waas, E. M. Arruda, J. Kieffer, M. D. Thouless, N. A. Kotov, *ACS Nano* **2011**, *5*, 6945.
[64] M. Iijima, H. Kamiya, *Colloids Surf., A* **2015**, *482*, 195.
[65] J. Zhu, W. Cao, M. Yue, Y. Hou, J. Han, M. Yang, *ACS Nano* **2015**, *9*, 2489.
[66] J. Fan, Z. Shi, M. Tian, J. Yin, *RSC Adv.* **2013**, *3*, 17664.
[67] Q. Kuang, D. Zhang, J. C. Yu, Y. W. Chang, M. Yue, Y. Hou, M. Yang, *J. Phys. Chem. C* **2015**, *119*, 27467.
[68] K. Ariga, A. Vinu, Y. Yamauchi, Q. Ji, J. P. Hill, *Bull. Chem. Soc. Jpn.* **2012**, *85*, 1.
[69] G. Decher, J. B. Schlenoff, *Multilayer Thin Films: Sequential Assembly of Nanocomposite Materials*, Wiley-VCH, Weinheim, Germany **2006**.
[70] Q. Xi, X. Chen, D. G. Evans, W. Yang, *Langmuir* **2012**, *28*, 9885.
[71] J. Wang, H.-B. Yao, D. He, C.-L. Zhang, S.-H. Yu, *ACS Appl. Mater. Interfaces* **2012**, *4*, 1963.
[72] J. Huang, T. Kunitake, S.-Y. Onoue, *Chem. Commun.* **2004**, 1008.
[73] L. Qiu, J. Z. Liu, S. L. Y. Chang, Y. Wu, D. Li, *Nat. Commun.* **2012**, *3*, 1241.
[74] S. Han, D. Wu, S. Li, F. Zhang, X. Feng, *Adv. Mater.* **2014**, *26*, 849.
[75] N. Jayaprakash, J. Shen, S. S. Moganty, A. Corona, L. A. Archer, *Angew. Chem.* **2011**, *123*, 6026.
[76] L. Jiang, Z. Fan, *Nanoscale* **2014**, *6*, 1922.
[77] Y. Lvov, S. Yamada, T. Kunitake, *Thin Solid Films* **1997**, *300*, 107.
[78] K. Ariga, Q. Ji, J. P. Hill, Y. Bando, M. Aono, *NPG Asia Mater.* **2012**, *4*, e17.
[79] J. I. Park, T. D. Nguyen, G. de Queirós Silveira, J. H. Bahng, S. Srivastava, G. Zhao, K. Sun, P. Zhang, S. C. Glotzer, N. A. Kotov, *Nat. Commun.* **2014**, *5*, 3593.
[80] Y. Xia, T. D. Nguyen, M. Yang, B. Lee, A. Santos, P. Podsiadlo, Z. Tang, S. C. Glotzer, N. A. Kotov, *Nat. Nanotechnol.* **2011**, *6*, 580.
[81] E. Piccinini, D. Pallarola, F. Battaglini, O. Azzaroni, *Mol. Syst. Des. Eng.* **2016**, *1*, 155.
[82] H. Feng, Y. Yang, Y. You, G. Li, J. Guo, T. Yu, Z. Shen, T. Wu, B. Xing, *Chem. Commun.* **2009**, 1984.
[83] Y. N. Kwon, J. O. Leckie, *J. Memb. Sci.* **2006**, *282*, 456.
[84] H. Jiang, K. Moon, Y. Li, C. P. Wong, *Chem. Mater.* **2006**, *18*, 2969.
[85] J. Im, J. Singh, J. W. Soares, D. M. Steeves, J. E. Whitten, *J. Phys. Chem. C* **2011**, *115*, 10518.
[86] M. Schlesinger, M. Giese, L. K. Blusch, W. Y. Hamad, M. J. MacLachlan, *Chem. Commun.* **2015**, *51*, 530.
[87] A. Acreman, M. Kaczmarek, G. D'Alessandro, *Phys. Rev. E* **2014**, *90*, 012504.
[88] G. C. Psarras, *Composites, Part A* **2006**, *37*, 1545.
[89] M. Powell, *Phys. Rev. B* **1979**, *20*, 4194.
[90] S.-Y. Fu, X.-Q. Feng, B. Lauke, Y.-W. Mai, *Composites, Part B* **2008**, *39*, 933.
[91] L. He, S. C. Tjong, *RSC Adv.* **2015**, *5*, 15070.
[92] G. D. Liang, S. P. Bao, S. C. Tjong, *Mater. Sci. Eng., B* **2007**, *142*, 55.
[93] J. Lee, P. Lee, H. Lee, D. Lee, S. S. Lee, S. H. Ko, *Nanoscale* **2012**, *4*, 6408.
[94] L.-J. Huang, N.-F. Ren, B.-J. Li, M. Zhou, *Acta Metall. Sin.* **2015**, *28*, 281.
[95] K.-Y. Chun, Y. Oh, J. Rho, J.-H. Ahn, Y.-J. Kim, H. R. Choi, S. Baik, *Nat. Nanotechnol.* **2010**, *5*, 853.

[96] J. R. Greer, R. A. Street, *Acta Mater.* **2007**, *55*, 6345.
[97] S. Vadukumpully, J. Paul, N. Mahanta, S. Valiyaveettil, *Carbon* **2011**, *49*, 198.
[98] P. Song, Z. Cao, Y. Cai, L. Zhao, Z. Fang, S. Fu, *Polymer* **2011**, *52*, 4001.
[99] N. D. Luong, U. Hippi, J. T. Korhonen, A. J. Soininen, J. Ruokolainen, L. S. Johansson, J. Do Nam, L. H. Sinh, J. Seppälä, *Polymer* **2011**, *52*, 5237.
[100] L. He, S. C. Tjong, *RSC Adv.* **2015**, *5*, 15070.
[101] N. D. Luong, N. Pahimanolis, U. Hippi, J. T. Korhonen, J. Ruokolainen, L.-S. Johansson, J.-D. Nam, J. Seppala, *J. Mater. Chem.* **2011**, *21*, 13991.
[102] X. Wang, H. Bai, Z. Yao, A. Liu, G. Shi, *J. Mater. Chem.* **2010**, *20*, 9032.
[103] J. Chen, R. Ramasubramaniam, C. Xue, H. Liu, *Adv. Funct. Mater.* **2006**, *16*, 114.
[104] G. Gorrasi, M. Sarno, A. Di Bartolomeo, D. Sannino, P. Ciambelli, V. Vittoria, *J. Polym. Sci., Part B: Polym. Phys.* **2007**, *45*, 597.
[105] A. Allaoui, S. Bai, H. M. Cheng, J. B. Bai, *Compos. Sci. Technol.* **2002**, *62*, 1993.
[106] T. McNally, P. Potschke, P. Halley, M. Murphy, D. Martin, S. E. J. Bell, G. P. Brennan, D. Bein, P. Lemoine, J. P. Quinn, *Polymer* **2005**, *46*, 8222.
[107] Y.-K. Choi, K. Sugimoto, S.-M. Song, Y. Gotoh, Y. Ohkoshi, M. Endo, *Carbon* **2005**, *43*, 2199.
[108] S. M. Yuen, C. C. M. Ma, Y. Y. Lin, H. C. Kuan, *Compos. Sci. Technol.* **2007**, *67*, 2564.
[109] W. Hu, S. Chen, Z. Yang, L. Liu, H. Wang, *J. Phys. Chem. B* **2011**, *115*, 8453.
[110] B. Zhang, D. Q. Zhao, M. X. Pan, W. H. Wang, A. L. Greer, *Phys. Rev. Lett.* **2005**, *94*, 1.
[111] A. Inoue, T. Zhang, K. Kita, T. Masumoto, *Mater. Trans.* **1989**, *30*, 870, .
[112] Y. Liu, S. Hata, K. Wada, A. Shimokohbe, *Jpn. J. Appl. Phys.* **2001**, *40*, 5382.